

A FULL POTENTIAL EQUATION SOLVER BASED ON THE ALGEBRAIC MULTIGRID METHOD: ELEMENTARY APPLICATIONS

SHLOMY SHITRIT* AND DAVID SIDILKOVER*

Key words. algebraic multigrid, transonic flow, full potential equation

Abstract. This article reports the development of an efficient, and robust full potential equation (FPE) solver for transonic flow problems, which is based on the algebraic multigrid (AMG) method. AMG method solves algebraic systems based on multigrid principles but in a way that it is independent on the problem's geometry. The mathematical difficulties of the problem are associated with the fact that the governing equation changes its type from elliptic (subsonic flow) to hyperbolic (supersonic flow). The flow solver is based of the body-fitted structured grid approach in complex geometries. We demonstrate the AMG performance on various model problems with different flow speed from subsonic to transonic conditions. The computational method was demonstrated to be capable of predicting the shock formation and achieving residual reduction of roughly an order of magnitude per cycle, both for elliptic and hyperbolic problems.

1. Introduction. A need for efficient and accurate solvers for compressible flow equations exists in many areas of engineering and science. A necessity to answer this need is what keeps motivating the development of such solvers for several decades starting from the beginning of computer age. Research on potential flow was conducted throughout the 1970s and into the early 1980s. By the beginning of 1970s. One of the major early breakthroughs in this development was the work by Murman and Cole on numerical solution of the small disturbances equation for transonic flow [1]. The key achievement of the work was the realization that since the governing equation changes its type from elliptic to hyperbolic where the flow reaches supersonic speeds, this should be reflected in the discretization of the equation. Their paper laid the ground work for the years that follows. It seems, however, that this direction was abandoned while still being in its infancy following another groundbreaking work of Jameson Schmidt and Turkel [2], in which a method for solving the Euler equations was devised. This methodology was generalized further to Navier-Stokes equations, turbulent flows, etc., and became the de-facto standard accepted by the aerospace industries in the most of the world until this day. However, in order to facilitate further progress, especially in improving its efficiency, Brandt [3] recommended to use the idea of factorization approach. This idea was successfully realized in the past for the incompressible high Reynolds number flow equations [4, 5], but the progress toward applying it to the compressible flow was rather slow and the success was very limited, considering several difficulties. One such difficulty is that the standard discretization schemes in multidimensions introduce non-physical coupling between the different co-factors of the system. This difficulty is addressed by the emerging class of the so called *factorizable* methods [6]. With this respect, the task of constructing an efficient FPE solver attains a great importance, since such a solver can be used not only by itself, but becomes an integral part of the overall methodology for solving the flow equations based upon the factorisable discretization.

One of the first multilevel methods toward solving partial differential equations fast and efficiently is the multigrid method. This method is attractive since large scale sparse algebraic systems of equations can be solved in nearly optimal scaling. There are two multigrid approaches: geometric and algebraic. In 1964, Fedorenko [7] introduced the first instance of a class of algorithms that would come to be known as multigrid methods [8, 9]. Since then, other mathematicians extended Fedorenko's idea to general elliptic boundary value problems with variable coefficients; see e.g., [10]. However, the full efficiency of the multigrid approach was realized after the works of Brandt [11, 12]. He also made these methods applicable to nonlinear problems by introducing the Full Approximation Scheme (FAS) [12]. Another achievement in the formulation of multigrid methods was the Full Multigrid (FMG) scheme [12, 13], based on the combination of nested iteration techniques and multigrid methods.

In geometric multigrid methods the coarse-grids are uniformly coarsened or semi-coarsened, thus the freedom in the selection of the coarse-grids is limited. The grids hierarchy is constructed based on the grid geometry information rather than properties of the difference operator. In addition, the

*Soreq NRC, Yavne 81800, Israel

definition of smoothness of the error involves grid geometry. These geometric dependency limits the problems it can be used to solve. Furthermore, geometric multigrid are in general not robust with respect to the operator coefficients. For problems where algebraic multigrid an irregular complex grids are involved (Anisotropies which are a result either the grid or the equation itself) the implementation of the geometric multigrid is definitely practically impossible. In the 1980s AMG methods were developed [14, 15, 16, 17] to deal with these problems by extending the main ideas of geometric multigrid methods to an algebraic setting. AMG is a method for solving algebraic systems based on multigrid principles with no explicit knowledge of the problem geometry. AMG uses the matrix’s properties to construct the operators involved in the algorithm. The AMG framework usually uses a simple pointwise relaxation method whose role is to smooth (in the algebraic sense) the error and then attempts to correct the algebraically smooth error that remains after relaxation by a coarse-level correction.

The purpose of this work is to develop a structured FPE solver which is based on the AMG method. The practical goal of this is twofold: First, to develop an important building block for the factorizable methodology. Second, to develop a stand-alone “optimally” efficient FPE solver. The flow solver is to be capable to deal with flow ranging from subsonic to transonic conditions. Such a solver can be a useful tool for engineers during the design process where multiple computations need to be performed as small changes to the geometry are made. The paper is organized as follows: Background on the classical AMG method is given in Section 2. The transonic flow problem is introduced in Section 3. Numerical calculations for body-fitted structured grids are presented in Section 4 and convergence results for various flow speeds are given.

2. Classical AMG – concept and description. We address the reader to [16, 18, 19] for a detailed description of the AMG algorithm, while in this paper we shall only briefly review the algorithm and emphasizing its aspects. In this paper we assume the reader to have some basic knowledge of the “traditional” geometric multigrid. He should be familiar with smoothing and coarse-grid correction process, and with the recursive definition of multigrid cycles. We limit our discussion to the basic principles of the AMG method. We shall give here a brief description of the classical AMG in the spirit of [16] followed by a description of the solution process. Regarding more detailed information on geometric and algebraic multigrid, we refer to [20, 21] and the extensive list of references given therein.

Consider a certain boundary-value problem for a scalar PDE in domain Ω . Its discretization will result in a linear algebra problem of the form $Au = f$, where A is an $n \times n$ matrix with entries a_{ij} with $i = 1, \dots, n, j = 1, \dots, n, u = \{u_j\}$ is the vector of unknowns, $b = \{b_j\}$ is the forcing term vector and n is the number of points in the computational grid covering the domain.

In geometric multigrid the definition of smoothness of the error involves grid geometry. The absence of grids in AMG renders this definition meaningless. Therefore, the concept of smoothness has to be generalized to some meaningful measurable quantity which can be computed based on the discrete operator only. A common definition of the algebraic smoothness is based on the fact that a simple pointwise relaxation scheme, like symmetric Gauss-Siedel (SGS), damps effectively high oscillatory modes of the error only. Consequently, the coarse-grid correction must deal with the remaining slow components. The characterization of such slow components, e , is: $Ae \simeq 0$.

2.1. Coarsening process. In the context of an algebraic multigrid we are going to deal at each level with a linear system of equations

$$A^m u^m = f^m, \tag{2.1}$$

where m is the level index. The goal is to split variables into two groups: those remaining on the coarse-level (C) and those that can be “represented” by the coarse-points and, therefore, may not be included into the coarse-level (belong to $F \setminus C$). The coarsening process is derived based on the strong and weak connections between unknowns, which essentially measure the relative size of the off-diagonal entries. Connections between neighboring variables considered strong if the size of the corresponding matrix entry exceeds a certain threshold, relative to the maximum entry of the row. This threshold value is very important for constructing a good coarse-grid. According to [16] a point i is said to be strongly connected to point j if

$$-a_{i,j}^m \geq \varepsilon \max(-a_{ik}^m). \quad (2.2)$$

The threshold value ε is kept fixed for most applications, with a typical value of 0.25. It was found that for the problems considered here this approach can lead to an inadequate coarsening and interpolation processes and hence lead to poor convergence. Therefore, a dynamic threshold approach was devised, and for further details we refer the reader to [20].

2.1.1. Restriction and interpolation operators. Having constructed the coarse-levels, we need to devise the restriction (residual transfer) and prolongation (correction interpolation operators). According to the classical AMG approach (see [16] for details) one can design the prolongation operator I_m^{m+1} , while the restriction operator is taken to be the transposed of the prolongation

$$I_{m+1}^m = (I_m^{m+1})^T. \quad (2.3)$$

For the purpose of this work, however, this procedure had to be modified so that the prolongation operator is devised directly according to certain rules (see [20]).

2.1.2. Restriction and coarse-level operators. In the standard approach, suggested by Ruge and Stueben [16], the restriction operator is defined as the transpose of the interpolation, I_{m+1}^m, I_m^{m+1} . Then the coarse-level operator is defined by the Galerkin type algorithm,

$$A^{m+1} = I_m^{m+1} A^m I_{m+1}^m. \quad (2.4)$$

This is the simplest way to construct the restriction and coarse-level operators. However it is known (see, for instance [22]) that it may lead to poor convergence, when the matrix A^m is not an M-matrix, which is normally the case for the problems considered in this work. Therefore, some alternatives had to be considered (see [20]).

2.1.3. Solution phase. The solution phase of the algorithm relies on the resulting operators to perform an iterative solution process (AMG cycles) until a desired level of accuracy is reached. An AMG cycle can be described in the following as consisting of the following stages:

1. Pre-smoothing by a relaxation method like Jacobi or Gauss-Seidel
2. Performing restriction of the problem, i.e., transferring residuals to the coarser-level.
3. Solution on the coarse-level (by recursion).
4. Performing prolongation, i.e., interpolating the solution correction to the finer level.
5. Post-smoothing, again, by a certain relaxation method.

2.1.4. Smoothing. Usually, the relaxation used as an ingredient of an AMG algorithm is a pointwise one. One of the central contributions of our approach is developing a stable pointwise direction-independent relaxation for the entire range of the flow speed, from low Mach number flow up until transonic and supersonic regimes. This development was a prerequisite for considering application of AMG to the transonic flow problem. For further details we refer the reader to [20].

2.1.5. Measuring the algorithm efficiency. The computational complexity concept is intended to measure an algorithms requirements for computer resources: computer storage (memory), and CPU time. There are three types of complexity measure that are commonly considered: convergence rate, grid complexity, and operator complexity.

Convergence factor: the rate in which the residual is decreased between consecutive V-cycles. This parameter gives an indication of how many iterations are needed in order reduce the residual to a sufficient level.

Grid complexity: is the total number of elements in the coarse-levels divided by the number of elements in the fine level. Let n_{Ω}^k denote the number of degrees of freedom on level k and n_L^k the number of nonzero entries in the level k and operator A^k . Therefore, the grid complexity is given by

$$C_{\Omega} = \frac{\sum_{k=1}^m n_{\Omega}^k}{n_{\Omega}^1}. \quad (2.5)$$

The grid complexity provides a direct measure for the storage required for the solution and right hand side vectors and it is a useful tool to compare different coarsening strategies. In geometric multigrid, if coarse-grids are constructed by halving the number of points in each dimension, the grid complexities for one, two, and three dimensions are 2, 4/3 and 8/7, respectively [18].

Operator complexity: is defined as the sum of the number of nonzero matrix elements in all the coarse-levels, divided by the number of the nonzero matrix elements in the fine-level. It is defined as follows:

$$C_L = \frac{\sum_{k=1}^m n_L^k}{n_L^1}. \quad (2.6)$$

The amount of work required by the relaxation and residual computations is directly proportional to the number of the nonzeros in the coarse-levels. Therefore, small values of the operator complexity that increase linearly with the problem's resolution signifies a linear complexity operator.

3. The FPE discretization – general idea. Transonic flow can be described by the FPE which is derived from the Euler equations by assuming that the flow is inviscid, isentropic, and irrotational. This potential flow will be treated in the conservation form:

$$\frac{\partial}{\partial x}(\rho u) + \frac{\partial}{\partial y}(\rho v) = 0, \quad (3.1)$$

where u and v are the velocity components in the Cartesian coordinates x and y , respectively, and ρ is the density. The velocity components are the gradient of the potential ϕ ,

$$u = \frac{\partial \phi}{\partial x}, \quad v = \frac{\partial \phi}{\partial y}. \quad (3.2)$$

The density ρ is computed from the isentropic formula:

$$\frac{\rho}{\rho_\infty} = \left(1 + \frac{\gamma - 1}{2} (V_\infty^2 - \phi_x^2 - \phi_y^2)\right)^{\frac{1}{\gamma - 1}}, \quad (3.3)$$

where γ is the ratio of specific heats and V_∞ is the free-stream velocity and ρ_∞ is the free-stream density. The relation between the local speed of sound a and the flow speed is defined by Bernoulli's equation:

$$a = \left(a_\infty^2 - \frac{\gamma - 1}{2} (V_\infty^2 - \phi_x^2 - \phi_y^2)\right). \quad (3.4)$$

The discretization of the FPE in the conservation form is based on the same rational which was applied in the quasi-linear case, and for this purpose we address the reader to our previous work [20, 21] for a detailed description. In this section we shall only briefly review the general idea of the discretization.

The strategy of discretizing the FPE in the conservation form is based on the rotated difference approach introduced by Jameson [23] and was developed for the quasi-linear form. However, this approach is not implemented directly. Instead, it is accomplished indirectly by following the same rational. We start from from the FPE in the quasi-linear form that can be formulated as,

$$\nabla^2 \phi - M^2 \frac{\partial^2}{\partial s^2} \phi = 0. \quad (3.5)$$

Let us look at both terms. Note that when the Mach number is close to zero (incompressible flow) the second term can be neglected and we are left with Laplacian $\nabla^2 \phi$ which is discretized by a central differencing, according to [20]. As the Mach number is increased, the second term which describes the second derivative in the streamwise direction, actually determines the “dynamics” of

the flow. Thus, in the discretization of the FPE in the conservation form we would like to apply the same rationale. Expanding the FPE and collecting the Laplacian terms, (3.5) can be formulated as,

$$\rho \nabla^2 \phi + \left(\phi_x \frac{\partial}{\partial x} + \phi_y \frac{\partial}{\partial y} \right) \rho = 0, \quad (3.6)$$

where the density ρ is given in (3.3). Note that (3.5) and (3.6) have a similar structure. The density parameter ρ plays two roles. In the first term it serves as a coefficient. In the second term it serves as an unknown variable. As one can see, the second term in the above both equations are identical. Therefore, the same rationale applied in the quasi-linear case can be applied to the conservation form. The description of the discretization technique is as follows: For the first term $\nabla^2 \phi$ the fluxes are computed by a central discretization independent on the flow direction and speed. The dynamic of the flow is reflected in the second term which is discretized in such a way that the results is a “wide” approximation in the streamwise direction.

4. Applications and performance. Several two dimensional flow calculations have been performed to test the performance of the AMG method implemented on the FPE under body-fitted structured grid configurations. Two dimensional solutions for the following problems will be presented: a channel with a circular bump, a circular cylinder with and without circulation, and flow through a convergent-divergent nozzle. The discrete approximation to the FPE in the subsonic flow regime is second order accurate in space and the supersonic region is first order accurate. We consider several measures of the efficiency of the algorithm. Our focus in the numerical experiments is on reducing the residual by at least ten orders of magnitude. This residual reduction measures the asymptotic convergence rate of the resulting cycle. A lower values requires fewer iterations in the solution phase. For each V-cycle C_f denotes the convergence factor, i.e., residual reduction by each V-cycle. The grid complexity and operator complexity are denoted by C_Ω and C_L , respectively.

The following default settings were used throughout the calculations, unless explicitly stated otherwise: The coarsening process including the construction of restriction operator is done according to Algorithm 2, described in [20] for all the problems that follow. The second-pass process was applied only for the fine-level in order to satisfy the interpolation requirements. Strong connectivity is defined by a fixed threshold $\varepsilon = 0.25$. The dynamic threshold was applied only where the fixed threshold fails. By default we use a symmetric Gauss–Seidel relaxation, two pre and two post smoothing steps being the default. The type of interpolation used is the one described in [20]. Coarsening is terminated as the number of points at the coarsest level drops below 1% of the total number of points on the finest level.

4.1. A channel with a bump.

4.1.1. Problem definition and boundary conditions. The height of the channel is L and length $3L$. Along the bottom wall there is a circular arc of length L and thickness $0.1L$. An H -grid is constructed, based on the algorithm of Blazek [24], using 96 cells in x -direction and 32 cells in the y -direction, as presented in Figure 4.1. A constant velocity (and Mach number) as inlet and outlet flow conditions were imposed. At the top and bottom, a solid wall boundary condition was applied. A uniform free-stream V_∞ was imposed as an initial condition.

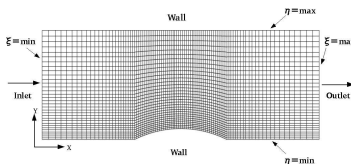


Figure 4.1: Mesh 96×32 used for the channel flow test case.

4.1.2. Qualitative results. The Mach number isolines and color maps are shown in Figure 4.2. The problems were solved for the following Mach numbers: 0.01, 0.25, 0.5, and 0.64. One isoline has been drawn on the color map every 0.013 ranging from 0.0 to 0.65. It is clear that within the low Mach number range, the solution does not greatly depend on the Mach number and the Mach isolines are practically identical. When M_∞ is increased, the compressibility effects become more dominant and for an incident velocity of $M_\infty = 0.64$ a supersonic region terminated by a shock (see Figure 4.2(d) appears above the bump. The pressure coefficient for the four cases described above is presented in Figure 4.3. The shock jump is clearly visible in the pressure distribution when $M_\infty = 0.64$.

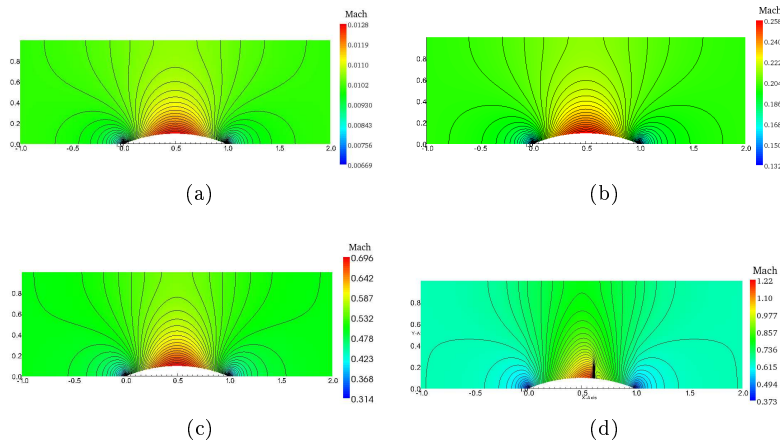


Figure 4.2: Mach number isolines computed on the (96×32) mesh for the following free-stream Mach numbers: a) $M_\infty = 0.01$, b) $M_\infty = 0.25$, c) $M_\infty = 0.5$, d) $M_\infty = 0.64$. Observe the shock appearing at $M_\infty = 0.64$.

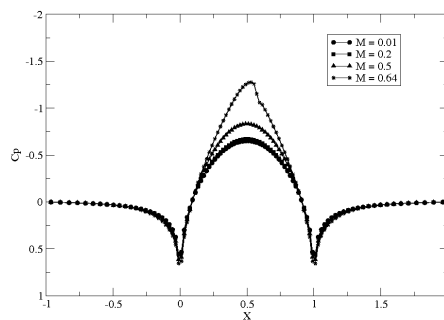


Figure 4.3: The pressure coefficient C_p calculated at the bottom wall for $M_\infty = 0.01 - 0.64$. Observe the shock appearing at $M_\infty = 0.64$.

4.1.3. AMG performance. The first coarse-level for each case described above is sketched in Figure 4.4. The case of $M_\infty = 0.01$ is characterized by a practically incompressible flow which results in nearly an isotropic equation. So, we would expect that the coarse-points would be distributed

uniformly at the entire flow field. However, as can be seen in Figure 4.4(a) this is not the case, while the reason for that is the irregularity (anisotropy) of the grid which is clearly reflected in the coarsening pattern. The coarsening algorithm is strongly influenced by the grid’s stretching in the x and y directions, adjacent to the bump. For example, the coarsening pattern above the bump is nearly isotropic since the cell’s aspect ratio is nearly unity, so the irregularity of the grid is not significant at this area. In addition, the discrete operator in this case relies upon a nine-point stencil which results in an “aggressive coarsening” (similar coarsening pattern can be obtained by solving the Poisson equation with a nine-point stencil). However, as we move further away from the bump in the y -direction the grid’s aspect ratio is increased since the cells are stretched in the x -direction. Consequently, a given change in the derivatives along the x -direction would influence the new solution stronger than the same change in the derivative along the y -direction. The problem shows strong dependence in the x -direction, and little or no strong dependence in the y -direction. The same process occurs in both sides of the bump, where the grid is coarsened in the y -direction – the direction of strong connections. This coarsening pattern for the rest of the flow conditions is essentially the same, except for $M_\infty = 0.64$ where a slight disturbance of the regular coarsening above the bump, where the anisotropy is largest, appears. It is important to mention here that a dynamic threshold was applied for this specific problem while in the rest subsonic cases a fixed threshold of $\varepsilon = 0.25$ results in good performance in terms of complexities and convergence properties.

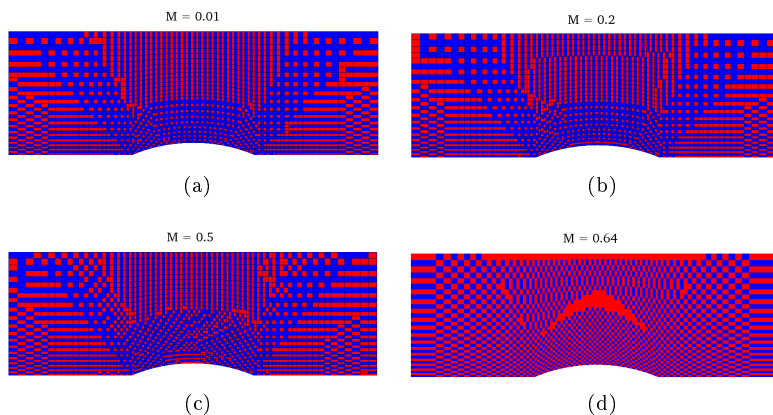


Figure 4.4: The finest and first coarse-level for flow through a channel with a bump. The mesh size is (96×32) . The problem was solved with various Mach numbers: a.) $M_\infty = 0.01$, b.) $M_\infty = 0.2$, c.) $M_\infty = 0.5$, d.) $M_\infty = 0.64$. The blue point corresponds to F -point (fine level) while the red point corresponds to C -point (coarse-level).

The convergence rate is shown in Table 4.1 for each V-cycle, in four different cases of M_∞ . Note that for the first three cases and for all the grid sizes, the convergence factor is bounded well below 0.1. The residual norm decreased by relatively the same factor with each V-cycle. This continues until it levels off after about ten V-cycles near 10^{-13} , where round-off error is of the order of the residual norm itself. Due to the mathematical nature of the potential equation, the free-stream Mach number has a large impact on the convergence rate. When the Mach number is increased, so does the upwind bias of the discretization, a decrease in the convergence rate occurs. In addition, the effect of the nonlinearity and the existence of shock waves manifest themselves in the convergence properties for $M_\infty = 0.64$, where the first three cycles are slow to converge and then the residual reduction is stabilized on 0.1 for the remaining 7 V-cycles. It is rather clear that this slow convergence is only caused by the strong nonlinearity and the presence of a discontinuity. It takes 2 – 3 “waste” cycles before the critical error components are sufficiently reduced by relaxations and the convergence becomes faster.

One possible way to improve the convergence rate at the beginning of the solution phase is by improving the initial condition. This can be achieved by the full multigrid (FMG) approach [8, 18]. The convergence of nonlinear iterations depends even more critically (compared to subsonic flow for instance) on a good initial condition. Typically, the better the initial condition used on the fine-level, the less significant is the effect of nonlinearity on the convergence and the more effective the fine-level solver will be. The FMG approach was implemented in this problem for subsonic and supersonic flow as well. For subsonic flow it worked pretty good, the interpolation $I_{m+1}^m A^{m+1}$ is generally accurate enough to be treated by the fine-level relaxation. However, for supersonic flow, where strong nonlinearity exist the success is very limited. It is very important to mention that although the first three cycles are slow to converge, in the remaining V-cycles the convergence rate is lower than 0.1 without any local smoothing sweeps around the shock waves. To illustrate the residual reduction graphically, Figure 4.5 presents the convergence history of the residual (L_2 -norm) versus the iterations number, for the four cases described above. We observe that for subsonic cases, $M_\infty = 0.1 - 0.5$ we need less than 10 V-cycles to reduce the L_2 -norm of the residual by 10 orders of magnitude. As for the transonic case of $M_\infty = 0.64$, the convergence is somewhat slower here while about 12 cycles are required to reduce the residual by 10 orders of magnitude.

Table 4.1: Convergence factor C_f , grid complexity C_Ω , and operator complexity C_L for four cases of Mach numbers.

complexities	$M_\infty = 0.01$	$M_\infty = 0.2$	$M_\infty = 0.5$	$M_\infty = 0.64$
C_f	0.03	0.04	0.04	0.10
C_Ω	1.58	1.60	1.72	2.06
C_L	2.15	2.25	3.24	3.56

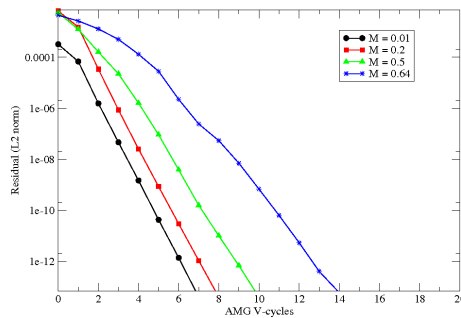


Figure 4.5: Convergence history of the discrete L_2 -norm of the residual for various cases of Mach numbers.

As already mentioned, compared to isotropic problems, complexity is generally higher for anisotropic problems. The complexities can increase further for problems as discussed here where anisotropies are not aligned with the grid. Table 4.1 presents the grid and operator complexity for four test cases of Mach number. In the case of $M_\infty = 0.01$ the grid complexity is 1.58. As the Mach number is increased the problem becomes strongly anisotropic and it results in an increased grid complexity. This is an expected behavior of the AMG algorithm since the memory (size of coarse-levels) requirement for strongly anisotropic problem is higher than that for isotropic problem. The reason is that AMG essentially performs one-dimensional coarsening in the direction of the

strong connections. Therefore, when $M_\infty = 0.64$ a large “pocket” of supersonic flow is obtained above the bump which is terminated by a shock wave. In this region, the anisotropy is largest, and the grid complexity is $C_\Omega = 2.06$.

The operator complexity is above 2 for the four cases of Mach number. The operator complexity reflects the cost of one relaxation sweep on all the levels. So, consider the case of $M_\infty = 0.01$, a $V(2, 2)$ cycle of AMG costs about 9.16 WUs (2.29WU on the descent and the ascent). The operator complexity increases slightly with the Mach number. It is clear that the operator complexity affects the number of operations per cycle and hence small operator complexity leads to low cycle times. Two possible reasons for the increased operator complexity are the average stencil size and the coarsening process. The average stencil size is the average number of coefficients per row. For simplicity, let us look at the fine-level. When $M_\infty \ll 1$, the stencil size of the matrix A^* is large, although, the matrix \hat{A} is diagonally dominant with $a_{i,j} \approx 1$ but the weights of the entries off-diagonal are definitely nonzero (it is zero for $M_\infty = 0$). As the Mach number increases so does the average stencil of A^* . It is possible to get very large stencil sizes on coarser levels (as will be discussed in Table 4.7). Large stencil size can lead to large operator complexity since various processes such as coarsening, interpolation and relaxation, require that neighbors of neighbors are visited which results in a growth in the number of operations per cycle. The second reason for the increased operator complexity is the relatively large number of points on the coarse-levels. Furthermore, the second-pass process, can also contribute to the relatively high complexities since F -points are replaced by C -points in order to satisfy the interpolation requirements.

A grid dependence study has been conducted to verify the independence behavior of the AMG algorithm on the grid resolution; two more grid levels have been used with (24×8) and (48×16) points. It is very important to mention that our main interest here is to verify the robustness of the code rather than achieving the highest possible efficiency. Therefore, at each resolution, the AMG components (for instance, dynamic threshold or second-pass process) were “fixed”, that is, they were not locally adjusted to particular requirements of a given case. The complexities are depicted in Table 4.2. It can be clearly seen that the algorithm is scalable and does not depend on the problem size (the convergence factor is nearly constant for all the grids considered).

Table 4.2: The table shows the results of the AMG V-cycles applied to the flow through a nozzle. The second norm of the residual $\|R^m\|_2$ after each V-cycle and the convergence factor C_f are detailed for two different mesh sizes 25×9 and 49×17 .

grid size \rightarrow	$M_\infty = 0.01$		$M_\infty = 0.2$		$M_\infty = 0.5$		$M_\infty = 0.64$	
	25×9	49×17	25×9	49×17	25×9	49×17	25×9	49×17
C_f	0.03	0.04	0.04	0.04	0.06	0.07	0.03	0.06
C_Ω	1.62	1.58	1.61	1.60	1.70	1.75	2.03	2.02
C_L	1.87	2.04	1.88	2.12	2.49	3.03	2.81	3.11

4.2. Flow around a circular cylinder.

4.2.1. Problem definition and boundary condition. We now consider a 2D cylinder placed in a uniform subsonic flow. The grid is sketched Figure 4.6 and its generation is straightforward in polar coordinates, formed by circles and radial lines. The outer boundary should be located far enough from the solid body in order to ensure that its influence is negligible, since we apply free undisturbed flow conditions on this boundary. In regions of strong flow variations (strong gradients) of the flow variables, near the cylinder wall, the grid is refined.

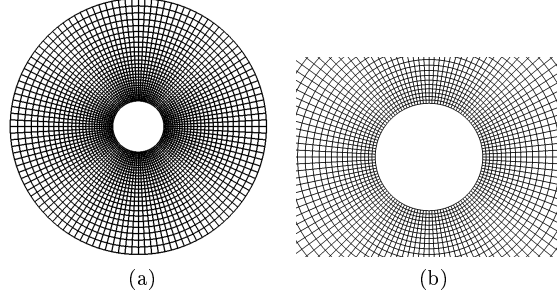


Figure 4.6: An O -type mesh used for the circular cylinder flow test case. a.) Extended mesh. b.) Close-up of the mesh around the cylinder.

The ξ -line is in the azimuthal direction and η -axis is in the radial direction. The boundary conditions imposed are as follows:

- The farfield boundary ($\xi = max$) is five times radius lengths away from the cylinder, where the inflow and outflow boundary conditions were applied. A uniform flow (Neumann condition) is imposed in the x -direction at the inlet and outlet regions of the domain. In practice, this condition was attained by projecting the velocity vector normal to the cell's face.
- A solid wall boundary condition is imposed on the cylinder's surface. The normal velocity is zero since no mass penetrates the solid body.
- At $j = 1$ and $j = j_{max}$, along the cut, a coordinate cut boundary condition was applied. This is a line composed of grid points with different computational indices but the same physical location. The grid is folded such that it touches itself. The cut boundary condition is implemented by using ghost cells. The situation is sketched in Figure 4.7. The ghost cells coincide location-wise with the grid cells on the opposite side of the cut. Hence the values of the potential in the ghost cells are obtained directly from the opposite cells. All the fluxes across the faces of the boundary cell are evaluated exactly like in the interior field. The cut boundary is implemented by generating a complete control volume at the cut. Using the ghost cells (Numbers 0 and 1 in Figure 4.7), the fluxes were calculated in the same way as inside the domain. The value of the first ghost cell (number 1) is obtained directly from cell number 4. The value of the second ghost cell (number 0) is obtained from cell number 3.

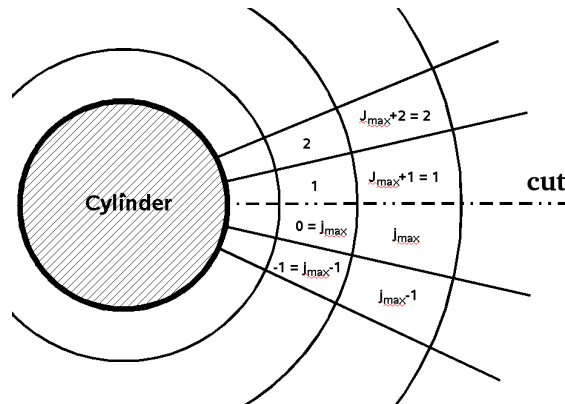


Figure 4.7: Coordinate cut boundary condition. Ghost cells are numbered as 0, 1, $(j_{max} + 1)$ and $(j_{max} + 2)$.

4.2.2. Qualitative results. The problem was solved for an inlet Mach number values ranging from 0.1 up to 0.41, and the results are presented in Figure 4.8. There are two stagnation points ($u \approx v \approx 0$) at $x = \pm a$, $y = 0$, at front and back of the cylinder. Within the low Mach number range, the solution does not greatly depends on the Mach number and practically it is similar to the incompressible flow. When the Mach number is increased the compressibility effect becomes more significant and for an inlet Mach number of 0.41, a sonic speed was reached on the top and bottom of the cylinder surface (symmetric), followed by a supersonic region terminated by a shock wave.

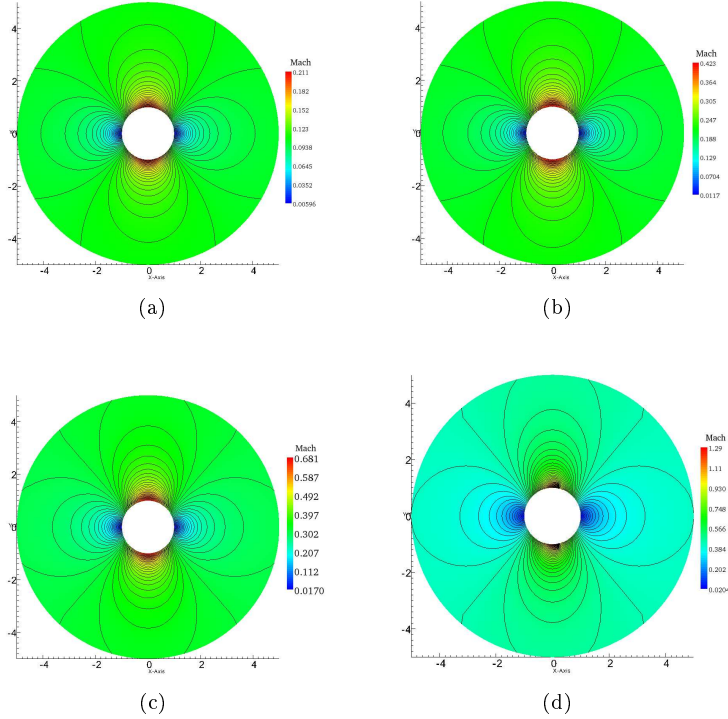
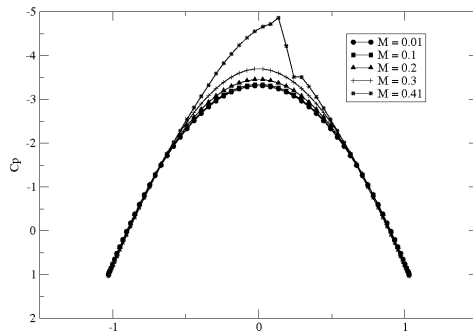


Figure 4.8: Distribution of velocity as computed on the (28×120) mesh, for an incident Mach number of: a.) $M_\infty = 0.1$, b.) $M_\infty = 0.2$, c.) $M_\infty = 0.3$, d.) $M_\infty = 0.41$. Observe the shock appearing at the top and bottom surfaces (case d).

The pressure distribution in a given flow pattern is of primary practical importance. A knowledge of the pressure distribution is necessary for the calculation of the forces and moments produced by the fluid on the solid boundaries. The pressure distribution at the cylinder surface can be found from Bernoulli's equation, $p + \frac{1}{2}\rho V^2 = const$. The pressure coefficient is defined as:

$$C_p = \frac{p - p_\infty}{\frac{1}{2}\rho U_\infty^2}, \quad (4.1)$$

where p_∞ represents the pressure at the farfield, and p is the pressure on the surface of the circular cylinder. The pressure coefficient distribution on the surface of the cylinder is plotted in Figure 4.9. Since C_p is symmetric about $x = 0$ and $y = 0$, there is no net force on the cylinder. Note that the pressure on most of the surface is less than p_∞ and the minimum value of C_p on the surface is -3 at $\theta = \pi/2$.



(a)

Figure 4.9: Surface pressure distribution along a circular cylinder with an incident Mach number ranging from $M_\infty = 0.01$ to $M_\infty = 0.41$, using the (28×120) mesh.

4.2.3. AMG performance. The first coarse-level for each case described above is sketched in Figure 4.10. It is important to mention that for all the subsonic cases described above, $M_\infty \leq 0.5$, a fixed threshold of $\varepsilon = 0.25$ was applied, since much better results were observed, especially in terms of grid and operator complexity. However, the situation is vastly different in the transonic case, $M_\infty = 0.41$, where a dynamic threshold was applied in order to achieve convergence. Although this fast convergence is achieved at the expense of an increased complexities (as is presented in Table 4.3), the alternative of a fixed threshold in this specific case results in divergence. This point emphasizes the robustness of the improved coarsening process in the AMG algorithm. When an incompressible flow is addressed, the operator is nearly isotropic – a nine-point stencil. Therefore, as expected, the points which construct the coarse-level are distributed uniformly, as can be seen in Figure 4.10(a). This type of coarsening is typical for nine-point stencils with all connections being strong, yielding grid complexity of ~ 1.6 . If a dynamic threshold is applied for this problem it would result in less “aggressive” coarsening, and the complexities would deteriorate slightly. However, we use the dynamic threshold where we really need it.

As the velocity is increased the equation becomes anisotropic, and this uniform coarsening structure holds until the flow reaches supersonic speeds. This extreme anisotropy is characterized by strong connection in the azimuthal direction (μ - axis). There is a slight deviation from the uniform coarsening in the upper and lower parts of the cylinder, where the anisotropy of the problem is most significant. However, the coarsening pattern is essentially the same.

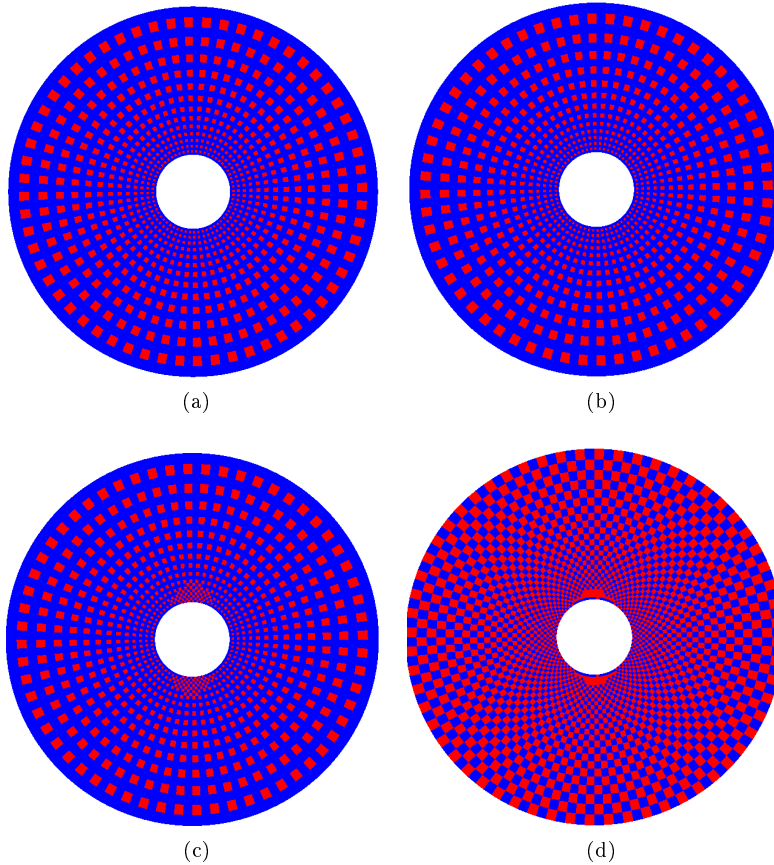


Figure 4.10: The finest and first coarse-level for mesh size (28×120) . The red color corresponds to the C -point and the blue color corresponds to F -point. The five flow conditions are as follows: a.) $M_\infty = 0.1$, b.) $M_\infty = 0.2$, c.) $M_\infty = 0.3$, d.) $M_\infty = 0.41$.

The residual reduction is sketched in Figure 4.11. Both the Mach contours and the convergence history are an evidence of the fact that the AMG solves the problem to the level of discretization on each grid. In the first three cases of $M_\infty = 0.01$, $M_\infty = 0.1$ and $M_\infty = 0.2$, the setup phase was performed, followed by 12 V-cycles. The convergence factors are bounded independent on the problem size. Solving the problem on reduced resolutions maintains the structure of the fine-scale problem and the convergence factor remains bounded independent on the problem size. In the case of $M_\infty = 0.3$, where the compressibility became significant, the results were obtained by repeating the setup phase six times while applying two V-cycles between each update. It results in a total of 12 V-cycles until the residual decreased to the desired level of $\sim 10^{-10}$. The transonic case proved to be a more difficult test for the algorithm. The convergence rate in the first three cycles deteriorated slightly due to the strong nonlinearity. Although the first three cycles are relatively slow to converge, in the remaining V-cycles the convergence rate is lower than 0.1.

The convergence histories for the five cases are depicted in Figure 4.11. The effect of the Mach number on the AMG performance is clearly shown. The case of $M_\infty = 0.41$ results in a supersonic flow regime which is terminated by a shock wave. Convergence is somewhat slower here. It requires nearly 12 V-cycles to decrease the L_2 -norm of the residual to a level of 10^{-10} , which is twice the number of cycles required in the case of $M_\infty = 0.01$.

The grid complexity and operator complexity are also presented in Table 4.3. It is clear that when the flow is subsonic the complexities are bounded. In the case of $M_\infty = 0.41$ the grid and

operator complexity are high, relative to our above requirements, while the reasons for the increased complexities are similar to those stated in the previous problem (channel with a bump). A possible way to improve the complexities is by aggressive coarsening. This approach was implemented but, as expected, the convergence became considerably slower (above 0.3). Aggressive coarsening not only, causes the smoothing to be less effective but also the interpolation to be significantly less accurate.

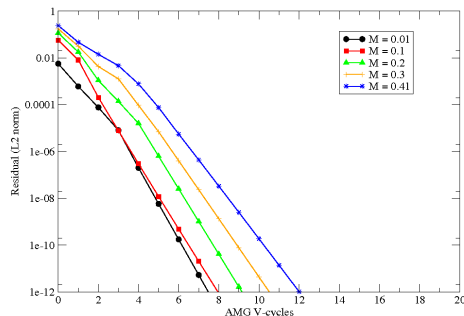


Figure 4.11: Convergence histories.

Table 4.3: Convergence factor C_f , grid complexity C_Ω , and operator complexity C_L for four cases of Mach number.

complexities	$M_\infty = 0.01$	$M_\infty = 0.1$	$M_\infty = 0.2$	$M_\infty = 0.3$	$M_\infty = 0.41$
C_f	0.06	0.06	0.04	0.06	0.07
C_Ω	1.31	1.33	1.33	1.33	1.98
C_L	1.82	1.867	2.26	2.18	3.09

This problem was solved for two more grids 14×60 and 7×30 , and the results are presented in Table 4.4. The convergence factors and complexities are bounded independent on the problem size. The grid complexity and operator complexity for grid 7×30 are $C_\Omega = 1.72$ and $C_L = 2.13$, respectively, and for the case of 14×60 , the complexities are $C_\Omega = 1.31$ and $C_L = 1.72$.

Table 4.4: The table shows the results of the AMG V-cycles applied to the flow around a circular cylinder. The second norm of the residual after each V-cycle $\|R^m\|_2$, convergence factor C_f , grid complexity C_Ω , and operator complexity C_L are presented for grid sizes 7×30 and 14×60 .

grid size \rightarrow	$M_\infty = 0.2$		$M_\infty = 0.41$	
	7×30	14×60	7×30	14×60
C_f	0.03	0.04	0.04	0.07
C_Ω	1.72	1.31	1.88	2.02
C_L	2.13	1.72	2.45	2.92

4.3. Flow around a circular cylinder with circulation.

4.3.1. Boundary conditions. Flow around a rotating circular cylinder is equivalent to the combination of flow past a cylinder and a vortex. Two aspects have drawn attention from researchers with respect to flow past a rotating cylinder. The first aspect is that the rotation action is able to suppress the separation of the boundary layer around the cylinder. The second aspect is the lift generated on the cylinder by the surrounding fluid, also known as Magnus effect [25, 26].

Exactly as the case of $\Gamma = 0$, there is an outer boundary where an inflow and outflow are applied. The circulation around the cylinder is applied by using the cut, emanating from the body to the farfield, where a jump in the potential is imposed. Thus, the cut can be interpreted as a periodic boundary with circulation, and it is defined as follows:

$$\begin{aligned}
 \phi_{i,0} &= \phi_{i,jmax} + \Gamma, \\
 \phi_{i,-1} &= \phi_{i,jmax-1} + \Gamma, \\
 \phi_{i,jmax+1} &= \phi_{i,1} - \Gamma, \\
 \phi_{i,jmax+2} &= \phi_{i,2} - \Gamma.
 \end{aligned}
 \tag{4.2}$$

The results are presented for the fine-level which includes 3360 grid points. The algorithm was tested by several flow conditions as follows:

1. $M_\infty = 0, \Gamma = 0.01$
2. $M_\infty = 0.1, \Gamma = 0.01$
3. $M_\infty = 0.1, \Gamma = 0.05$
4. $M_\infty = 0.1, \Gamma = 0.1$
5. $M_\infty = 0.4, \Gamma = 0.1$

The first step was to validate the problem setup, the choice of the boundary conditions, and the mesh attributes. It is accomplished by imposing a circulation $\Gamma = 0.01$ with zero free-stream ($M_\infty = 0$, case 1). The positive sign of the circulation, imposes a flow in the clockwise direction. The Mach isolines for this case are plotted in Figure 4.12. Since a zero free-stream is applied, the Mach contours are symmetric around the cylinder. The problem solved for an inlet Mach number values ranging from 0.01 up to 0.4, and the results are presented in Figure 4.13. Only the fourth case results in a supersonic flow regime. Notice that the stagnation point lies above the cylinder, in the region where the direction of the free-stream opposes the circulation. As the flow's speed at the surface of the cylinder increases, the region of close isolines around the cylinder extends far from the wall and, as a consequence the stagnation point moves upward.

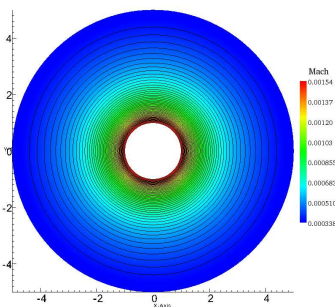


Figure 4.12: Flow over a cylinder having a circulation of $\Gamma = 0.01$. Contours are spaced for equal increments of 10^{-5} .

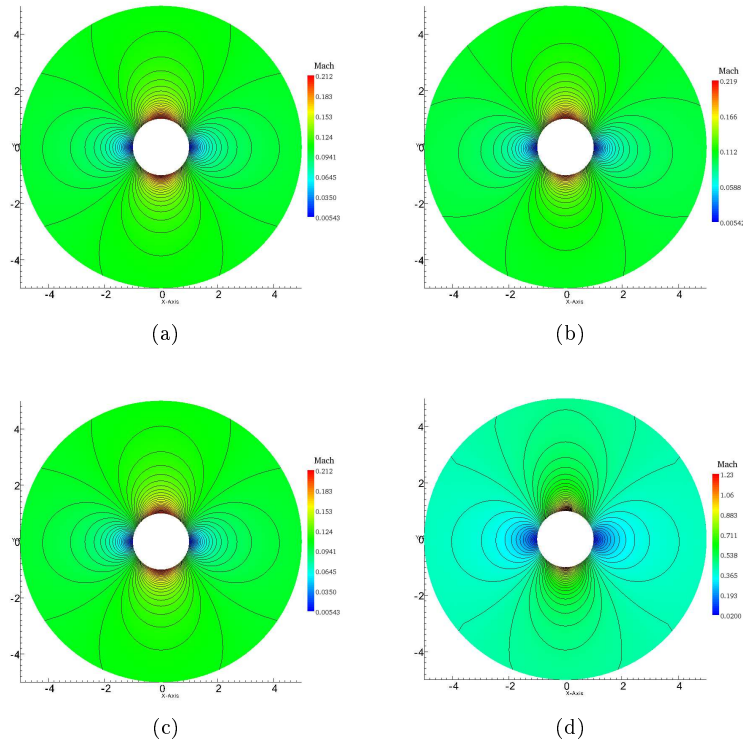


Figure 4.13: Distribution of velocity as computed on the (28×120) mesh, for the following flow characteristics: a.) $M_\infty = 0.1$, $\Gamma = 0.01$, b.) $M_\infty = 0.1$, $\Gamma = 0.05$, C.) $M_\infty = 0.1$, $\Gamma = 0.1$, D.) $M_\infty = 0.4$, $\Gamma = 0.1$. Observe the shock appearing at $M_\infty = 0.41$.

It was verified in these simulations that the velocity becomes close to the free-stream velocity along the outer boundary of the domain. The pressure coefficient C_p distribution on the surface of the cylinder is plotted in Figure 4.14. It is clear that when the flow is subsonic at the entire domain there is no significant difference in the C_p profiles. From Figure 4.14 we can see the pressure difference between the lower and the upper part of the cylinder. This is the lift generated on the cylinder by the surrounding fluid, also known as Magnus effect [26]. It is clear that the lift is increased with the free-stream velocity. As the flow becomes supersonic on the upper part of the cylinder's surface, a shock wave appears, and it is seen in the sharp decrease of C_p .

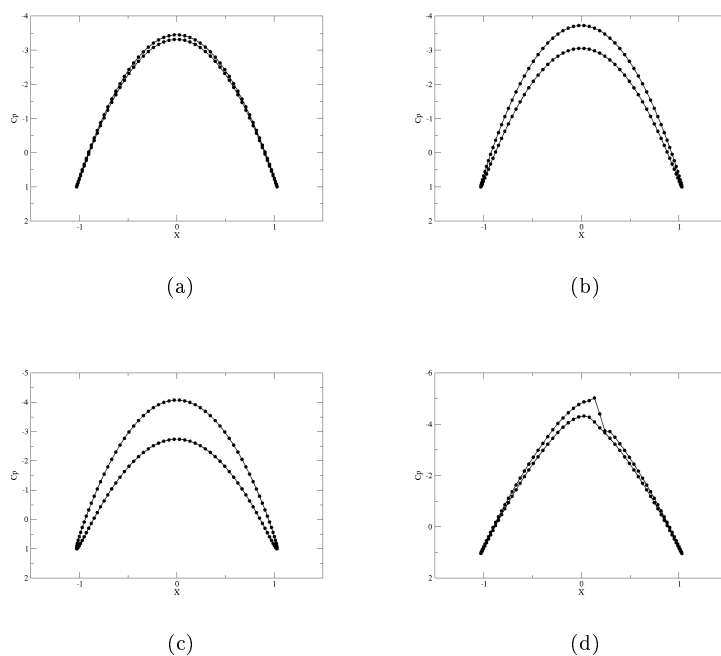


Figure 4.14: The distribution of pressure coefficient by using (28×120) mesh. The cases are as follows: a.) $M_\infty = 0.1$, $\Gamma = 0.01$, b.) $M_\infty = 0.1$, $\Gamma = 0.05$, C.) $M_\infty = 0.1$, $\Gamma = 0.1$, D.) $M_\infty = 0.4$, $\Gamma = 0.1$.

4.3.2. AMG performance. The first coarse-level for each case described above is sketched in Figure 4.15. When the flow is subsonic, $M_\infty < 0.5$, it is characterized by a nearly isotropic operator and the C -points which construct the coarse-level are distributed uniformly, as can be seen in Figure 4.15(a). As the free-stream becomes supersonic, as mentioned above, there is a slight disturbance of the uniform coarsening pattern where the anisotropy of the operator is largest (see Figure 4.15(e)).

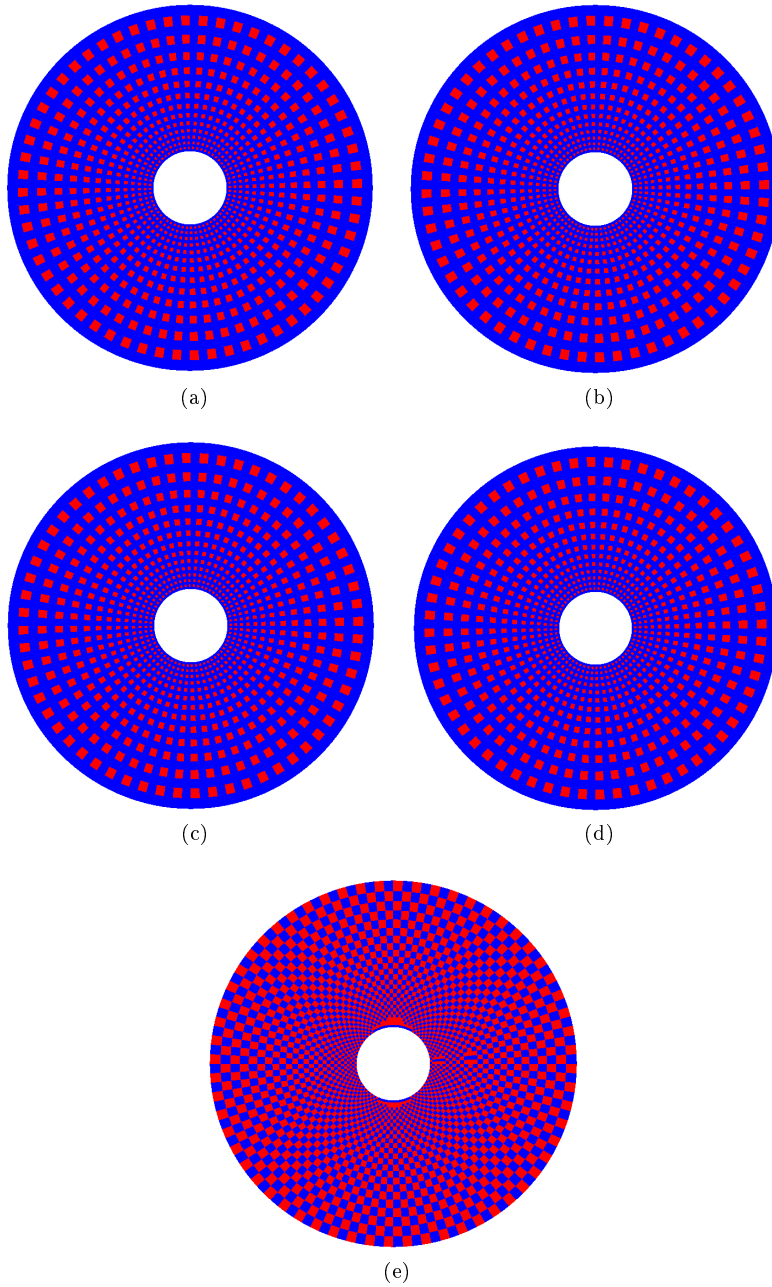


Figure 4.15: The finest and first coarse-level. The red color corresponds to the C -points while the blue color corresponds to the F -points. The mesh size is (28×120) . The five flow conditions are as follows: a.) case 1, b.) case 2, c.) case 3, d.) case 4, e.) case 5.

The convergence of the method is summarized in Table 4.5 for the five cases in consideration. Using the standard L_2 -norm we see that after 12 cycles, the residual reached 10^{-15} and the AMG converge rapidly for the cylinder with circulation as for the previous model problem, where we saw a convergence rate lower than an order of magnitude for all the cases that introduced before. The fastest cycle, $M_\infty = 0.1$ and $\Gamma = 0.05$, needs 11 steps to reduce the residual by ten orders of magnitude. In cases 1 – 4 no updates of the matrix A^* and the restriction and interpolation operators

where needed. In case 5, the nonlinearity is dominant which required to execute the setup phase six times with two V-cycles in between. It results in an overall of 12 V-cycles to reach convergence.

The complexities for these five cases are presented in Table 4.5. The operator complexity is below 2 for cases 1 – 4 where the flow is subsonic in the entire field. Case number 5 is characterized by a transonic flow on the upper part of the cylinder and the grid and operator complexities were increased to 1.97 and 3.0, respectively.

Table 4.5: Convergence factor C_f , grid complexity C_Ω and operator complexity C_L for five cases of Mach number and circulation magnitude.

complexities	case 1	case 2	case 3	case 4	case 5
C_f	0.04	0.07	0.07	0.07	0.09
C_Ω	1.31	1.31	1.31	1.31	1.97
C_L	1.82	1.82	1.82	1.82	3.016

4.4. Nozzle.

4.4.1. Problem definition and boundary condition. The rocket engine nozzle has three functions: to produce thrust, to conduct the exhaust gases back to the free-stream and to set the mass flow rate through the engine. The nozzle has a rectangular section. It is constructed of a flat bottom wall and a converging-diverging channel with a maximum angle of 30° at the top wall. The convergent part follows a curved contour while the contour of the divergent part is a straight line. The ratio of the inlet area to the throat area is $\frac{A_{in}}{A_{throat}} = 1.4114$ and the ratio of the exit area and the throat area is $\frac{A_{out}}{A_{throat}} = 1.5$. Figure 4.16 is the mesh used for the calculation. The mesh size is 96×48 and it is clustered close to upper and lower walls vertically and in the throat horizontally, with a stretching factor of 1.1.

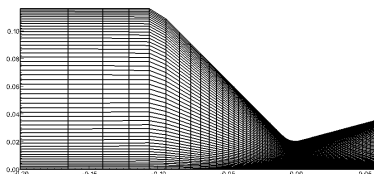


Figure 4.16: Mesh used for the converging-diverging nozzle flow test case.

The following boundary conditions were specified:

- A subsonic flow at the inlet and the same mass flow rate at the outlet, in the x -direction.
- Solid-wall boundary condition at the top and bottom walls.

4.4.2. Qualitative results. When the inlet velocity is not high enough to induce sonic flow in the throat, the flow in the nozzle is subsonic throughout. While for a subsonic inlet velocity of $M_\infty = 0.092$ the area ratio exactly equals the critical ratio A_{in}/A^* . The flow in the throat becomes sonic and a normal shock can be observed in the diverging section as can be seen in Figure 4.17. A strong pressure gradient is present in the case of $M_\infty = 0.092$, where a shock is obtained at the diverging section of the nozzle.

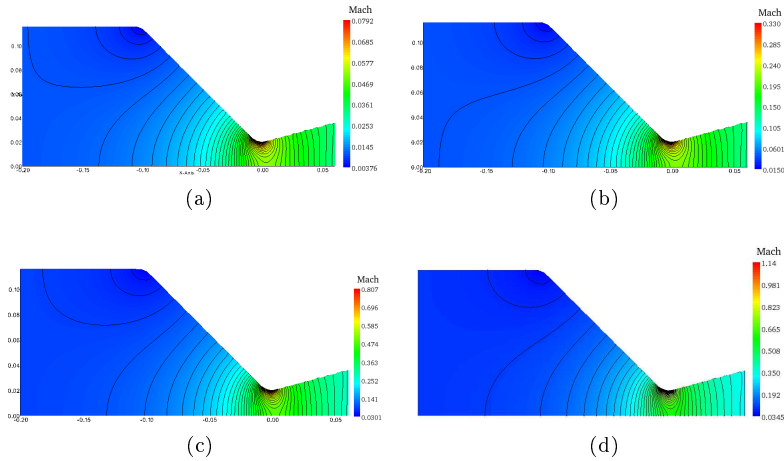


Figure 4.17: Distribution of velocity as computed on the (80×50) mesh, for the following velocities: a) $M_\infty = 0.01$, b) $M_\infty = 0.04$, c) $M_\infty = 0.08$, d) $M_\infty = 0.092$.

4.4.3. AMG performance. The first coarse-level for each case described above is sketched in Figure 4.18. A dynamic threshold was applied for all the following cases since a much stable performance were obtained, in terms of convergence properties, mainly in the transonic case of $M_\infty = 0.092$. Several observations are in order here. First, the coarsening pattern is not so intuitive for this specific problem since we would expect a uniform distribution of the coarse points at the inlet area, rather than a one-dimensional coarsening in the y -direction, at least for $M_\infty = 0.01$, where the equation is isotropic. A possible reason is the stretching of the grid cells in the x -direction which contributes to the strong connections in the y -direction, and thus, the AMG coarsening algorithm automatically coarsen in the direction of the strong connectivity. The one-dimensional coarsening pattern at the throat is exactly what we would expect to obtain, where the anisotropy is largest.

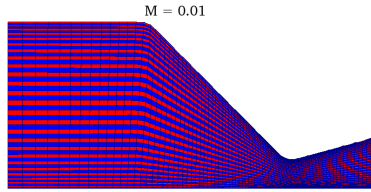


Figure 4.18: The finest and the first coarse-level for mesh size of (80×50) . The red color corresponds to the C -point and the blue color corresponds to F -point. This coarsening pattern was obtained for $M_\infty = 0.01$. The same coarsening pattern was obtained also for various flow conditions as follows: $M_\infty = 0.04$, $M_\infty = 0.08$ and $M_\infty = 0.092$.

The residual norm decreased rapidly for 10 to 12 V-cycles. We observe that each cycle exhibits a very stable convergence behavior with an asymptotic convergence rate of less than an order of magnitude. In the first case of $M_\infty = 0.01$, the setup phase was implemented only once, followed by 12 V-cycles. The case of $M_\infty = 0.04$, where the compressibility became significant, the results were obtained by repeating the setup phase 4 times while applying three V-cycles between each update. It results in a total of 12 V-cycles until the residual decreased to the desired level of $\sim 10^{-10}$. In the last two cases of $M_\infty = 0.08$ and $M_\infty = 0.092$ a more frequent updates of the matrices A , \tilde{A} , and the restriction and interpolation operators were needed in order to achieve efficient and

stable performance. In these cases, the setup phase was repeated six times while each update was followed by two V-cycles. It is important to note that the convergence rate in the first 2-3 cycles is not deteriorating significantly, compared to the previous problems, mainly due to a relatively good initial condition.

The grid complexity and operator complexity are also presented in Table 4.6. It is clear that the complexities are reasonable and bounded for all the flow velocities. In the case of $M_\infty = 0.01$ the second-pass process is applied for all the coarse-levels and it is well reflected in the grid complexity which is slightly increased to $C_\Omega = 1.98$.

The convergence histories for the five cases are depicted in Figure 4.19. The effect of the Mach number on the AMG performance is clearly shown. The case of $M_\infty = 0.092$ results in a supersonic flow regime which is terminated by a shock wave. The convergence is somewhat slower here. It requires nearly twice the number of V-cycles (10) to decrease the L_2 -norm of the residual to a level of 10^{-12} , compared to the case of $M_\infty = 0.01$. This slow convergence is mainly due to the 2 – 3 first “waste” cycles (slow to converge due to strong nonlinearity) until the convergence is stabilized.

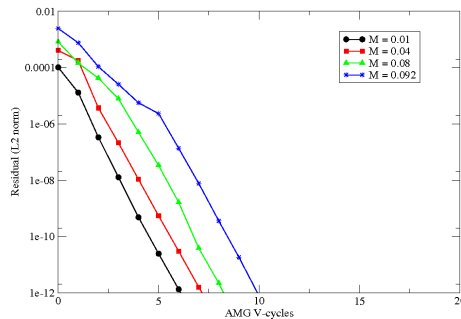


Figure 4.19: Convergence histories.

Table 4.6: Convergence factor C_f , grid complexity C_Ω , and operator complexity C_L for four cases of Mach number.

complexities	$M_\infty = 0.01$	$M_\infty = 0.04$	$M_\infty = 0.08$	$M_\infty = 0.092$
C_f	0.05	0.05	0.05	0.05
C_Ω	1.98	1.92	1.90	1.93
C_L	2.47	2.47	2.52	2.46

This problem was solved for two more cases of mesh size consist of 40×25 and 20×12 points. Both the L_2 -norm of the residual and the convergence factor for two different cases of $M_\infty = 0.01$ and $M_\infty = 0.092$ are presented in Table 4.7. Observe, that the difference in size of the above meshes hardly influence the convergence properties. As is already mentioned before, the computational work is determined by the operator complexity and the convergence factor. Only if both are bounded as a function of the problem size, we have an acceptable robust algorithm. In this case we can see that the complexities C_L and C_Ω are indeed independent of the grid size.

Let us examine the coarsening statistics. Table 4.7 presents the number of rows and the number of nonzeros for two cases of $M_\infty = 0.01$ and $M_\infty = 0.092$. The case of $M_\infty = 0.01$ was solved with seven levels (includes the fine-level) while the case of $M_\infty = 0.092$ was solved with four levels only. In the later case the coarsest level consists of a relatively large number of points, while the reason for

this is already pointed out before. The coarsening is not so aggressive and is similar for both cases. The first coarse-level is exactly half the number of points on the fine-level while this reduction ratio of grid points for the rest coarse-levels is approximately preserved. It is interesting to note here that although the stencil on the coarse-levels becomes larger, for both cases, subsequent coarsening does not become more aggressive. For both cases ($M_\infty = 0.092$ and $M_\infty = 0.01$) it happens simply because the dynamic threshold which tends to produce slightly larger coarse-levels. In case of $M_\infty = 0.01$ we can observe the additional effect of the second-pass process applied to all the coarse-levels. These two processes together contribute to the increase in grid and operator complexities but also to gain very efficient convergence properties.

Table 4.7: The table shows the results of the AMG V-cycles applied to the flow through a nozzle. The second norm of the residual after each V-cycle $\|R^m\|_2$ and the convergence factor C_f are detailed for two different mesh sizes.

grid size \rightarrow	$M_\infty = 0.01$		$M_\infty = 0.092$	
	20×12	40×24	20×12	40×24
C_f	0.09	0.10	0.08	0.07
C_Ω	1.90	1.91	1.75	1.85
C_L	2.03	2.28	2.09	2.38

Table 4.8: Results of the AMG V-cycles applied to the flow through the nozzle in various Mach numbers.

Level	Number of rows		Number of non-zeros		Average entries per row	
	$M_\infty = 0.01$	$M_\infty = 0.092$	$M_\infty = 0.01$	$M_\infty = 0.092$	$M_\infty = 0.01$	$M_\infty = 0.092$
A^m	4000	4000	69424	69424	17.3	17.3
A^{m+1}	2000	2000	37023	44173	18.5	22
A^{m+2}	968	983	26865	27449	27.7	27.9
A^{m+3}	449	504	17971	19374	40	38.4
A^{m+4}	205	268	8541	10661	41.6	39.7
A^{m+5}	91	-	3219	-	35.3	-

5. Conclusions. The FPE is useful for design and analysis of airfoil, wings, diffusers etc.. Computations are usually much less resource-consuming than those solving the Euler or Navier-Stokes equations. The FPE can be used for transonic flows, where a lot of design issues are of interest. Therefore, an efficient FPE solver can be of a substantial practical value. This work is concerning with developing such a solver. Transonic flow problem is a rather complex one from the computational point of view. One of the main difficulties is the fact that the differential operator changes its type between elliptic for subsonic flow regime and hyperbolic (with respect to the flow direction) in the supersonic flow regime. Another (sub-)difficulty is that the subsonic flow regime itself presents two extremities (and all the possible cases in between): nearly isotropic operator for the flow speed case and highly anisotropic operator for a nearly sonic flow speed. While the standard AMG algorithm can treat the latter difficulty.

The objective of this work was to develop a highly efficient solver for the FPE which would be able to compute transonic external and internal flows attaining a (nearly) linear computational complexity. The key innovation of this work is the solver's efficiency and also in the fact that it was achieved by means of adapting and applying the AMG approach to solving the problem. A 2D body-fitted structured grid solver which is based on the AMG method, was developed. To

take advantage of structured grid, the flow solver can deal with complex geometries in different resolutions. Several two dimensional flow calculations have been performed to test the performance of the AMG method under different flow conditions. The computational method was demonstrated to be capable of predicting the shock formation and achieving residual reduction of less than *an order of magnitude per cycle*, independent on the problem size.

REFERENCES

- [1] E.M. Murman and J.D. Cole. Calculation of plane steady transonic flows. *AIAA*, 9(1):114–121, Jan 1971.
- [2] A. Jameson, W. Schmidt, and E. Turkel. Numerical Solution of the Euler Equations by Finite Volume Methods Using Runge-Kutta Time Stepping Schemes. In *AIAA 14th Fluid and Plasma Dynamics*, volume 81-1259, Reston, VA 1981. AIAA.
- [3] A. Brandt. Multigrid techniques: 1984 Guide with Applications to Fluid Dynamics. The Weizmann Institute of Science, Rehovot, Israel, 1984.
- [4] I. Yavneh. *Multigrid Techniques for Incompressible Flows*. PhD thesis, The Weizmann Institute of Science, Rehovot, Israel, 1991.
- [5] A. Brandt and I. Yavneh. On multigrid solution of high-Reynolds incompressible entering flows. *Journal of Computational Physics*, 101:151–164, 1992.
- [6] D. Sidilkover. A factorizable scheme for the equations of fluid flow. *Appl. Numer. Math.*, 41:423–426, 2002.
- [7] R. P. Fedorenko. The Speed of Convergence of One Iterative Process. *USSR Comp. Math. Phys.*, 4:227–235, 1964.
- [8] U. Trottenberg, A. Schuller, and C. W. Oosterlee. *Multigrid*. Elsevier Academic Press, 2001.
- [9] P. Wesseling. *An Introduction to Multigrid Methods*. John Wiley & Sons, New York, 1992.
- [10] N.S. Bakhvalov. On the convergence of a relaxation method with natural constraints on the elliptic operator. *USSR Comput. Math. Math. Phys.*, 6:101, 1966.
- [11] A. Brandt. Multi-level adaptive technique (MLAT) for fast numerical solutions to boundary value problems. In *in Proc. 3rd Int. Conf. on Numerical Methods in Fluids Mechanics*, pages 82–89. Springer-Verlag, 1973. Lecture Notes in Physics 18.
- [12] A. Brandt. Multi-level adaptive solutions to boundary-value problems. *Math. Comput.*, 31:333–390, 1977.
- [13] W. Hackbusch. *Multigrid methods and applications*. Springer, 1985. Heidelberg.
- [14] A. Brandt, S. F. McCormick, and J. W. Ruge. Algebraic Multigrid (AMG) for sparse matrix equations. In *Sparsity and Its Applications*. Cambridge University Press, Cambridge, 1984.
- [15] A. Brandt. Algebraic multigrid theory: The symmetric case. *Appl. Math. Comput.*, 19:23–56, 1986.
- [16] K. Stueben. An introduction to algebraic multigrid. Technical report, German National Research Center for Information Technology (GMD), San Diego, 2001.
- [17] J. W. Ruge and K. Stueben. Algebraic Multigrid. In *Multigrid Methods*, volume 3, pages 73–130. S. F. McCormick, ed., SIAM, Philadelphia, 1987.
- [18] W. L. Briggs, V. E. Henson, and S. F. McCormick. *A Multigrid Tutorial*. Society for Industrial and Applied Mathematics, Philadelphia, 2 edition, 2000.
- [19] R. D. Falgout. An introduction to Algebraic Multigrid. In *Computing in Science and Engineering*. Lawrence Livermore National Laboratory, 2006.
- [20] S. Shitrit and D. Sidilkover. Toward applying algebraic multigrid to transonic flow problems. *SIAM Journal of Scientific Computing*, 32:2007–2028, July 2010.
- [21] S. Shitrit. *Transonic flow computations by Algebraic Multigrid*. PhD thesis, The Zandman-Slaner Graduate School of Engineering, Tel-Aviv University, Tel-Aviv University, July 2010.
- [22] Q. Chang, Y. Shu, and Wong H. Fu. On the Algebraic Multigrid. *Journal of Computational Physics*, 125:279–292, 1996.
- [23] A. Jameson. Iterative Solution of Transonic Flows Over Airfoils and Wings, Including Flows at Mach 1. *Pure. Appl. Math.*, 27:283–309, 1974.
- [24] J. Blazek. *Computational Fluid Dynamics: principles and applications*. Elsevier, 2001.
- [25] J. D. Anderson. *Fundamentals of Aerodynamics*. McGraw-Hill Science Engineering, 2005.
- [26] G. K. Batchelor. *An Introduction to Fluid Dynamics*. Cambridge University Press, 1967.